Evaluation and Comparison of Geomechanical Properties of Hydrate bearing and Frozen Sands

Muhammad Abbas, Jeffrey A. Priest & Jocelyn L. Hayley
Department of Civil Engineering – University of Calgary, Calgary, Alberta, Canada

ABSTRACT
This paper presents a set of experimental results on the geomechanical behavior of artificially synthesized methane gas-saturated hydrate bearing sands (HS), water-saturated hydrate bearing sands (WHS) and frozen sands (FS). HS was formed by injecting methane gas into the pore-space of partially saturated sand under pressure and temperature (PT) conditions that lie within the hydrate stability region. FS specimens were formed by freezing partially saturated sand specimens at -9 ºC for 24hrs. The changes in shear modulus during hydrate formation and water-saturation were monitored using a resonant column. Drained triaxial tests were carried out to determine large strain strength characteristics. Both HS and FS exhibited strain-softening behavior. HS gave greater peak strength than FS and showed different deformation characteristics. The hydrate was marginally dissociated in WHS during water-saturation and resulted in a major loss of strength. The findings provide useful new insights into the strength governing mechanisms in HS, WHS and FS.

Cette étude présente les résultats expérimentaux d'un test géo mécanique sur les hydrates de méthane, synthétisées artificiellement saturées de gaz (HS), les sables saturés d'eau (WHS) et des sables gelés (FS). HS a été formé en injectant le méthane dans l'espace poreux de sable partiellement saturé sous la pression et la température qui caractérisent la région de stabilité les hydrates. Les spécimens FS ont été formés en gelant les spécimens de sable partiellement saturés à-9 oC durant 24hrs. Les changements en module de cisaillement pendant la formation d'hydrate et la saturation d'eau ont été contrôlés en utilisant une colonne résonante. Les essais triaxiaux épuisés/drainés ont été menés afin de déterminer les caractéristique de force des souches des hydrates. HS, tel que FS, ont accusé quelques signes d adoucissement de tension. HS a donné une intensité maximale alors que FS et a montré de différentes caractéristiques de déformation. L'hydrate a été marginalement dissocié du WHS pendant la saturation d'eau, ceci a abouti à une perte majeure de puissance. Les conclusions de notre étude fournissent de nouveaux aperçus et perspectives utiles sur la force dirigeante des mécanismes des HS, WHS et FS.

1 INTRODUCTION

Methane hydrates (referred to as hydrates herein for simplicity) are crystalline solids formed of methane gas and water under high pressures and low temperatures. Methane hydrate reservoirs are abundant in nature and found below the seafloor along the continental margins and in the permafrost region where PT conditions for hydrate stability prevail.

Hydrates have attracted significant attention in recent years because of their potential promise to be a 'cleaner' energy resource in the near future. Estimates suggest that natural hydrates store twice the amount of organic carbon found in all other fossil fuels combined (Kvenvolden 1993). To realize this potential, dissociation of the hydrate is required to liberate the methane gas which can be achieved through depressurization, thermal stimulation or inhibitor injection (Moridis et al. 2004). As the presence of hydrate increases the strength and stiffness of geological sediments (Hyodo and Yoshimoto 2013; Miyazaki et al. 2010), the resulting dissociation will be accompanied by a loss of strength and an increase in pore pressure due to the evolution of gaseous methane. These processes have serious implications for well stability, blowouts and submarine landslides. Therefore, for gas production and hazard evaluation, it is imperative to characterize and understand the influence of different parameters on the mechanical response of hydrate bearing sediments and how they compare to the properties of the host sediments.

Limited characterization has been carried out to assess the mechanical behavior of natural hydrate bearing sediments due to the changes in pressure and temperature during extraction and transportation which can significantly alter the sediments original in-situ properties (Santamarina et al. 2012). Therefore, laboratory synthesis and testing of hydrate bearing soils have been the scope of most research studies to date.

From an energy perspective, about 10% of the global volume of natural hydrate is contained in sandy sediments (Collett et al. 2009) where the high concentrations and inherent permeability of the host sediment make them an ideal energy resource (Waite and Spangenberg 2013). Therefore, this study focusses on hydrates in sands. Numerous hydrate formation methods have been developed to artificially synthesize hydrate within sands including the ice seeding method (Stern et al. 1996), dissolved gas method (Spangenberg et al. 2005), excess gas method (Handa and Stupin 1992) and excess water method (Priest et al. 2009). Each of these methods gives rise to particular hydrate morphology that leads to different interactions with the host sediment. The excess gas method has been routinely utilized (Ghiassian and Grozic 2013; Hyodo et al. 2015, 2013a; Miyazaki et al. 2015), where a partially water-saturated sand specimen is pressurized with methane gas under hydrate-stable PT conditions for a

period of time that allows for the near-complete conversion of pore water into hydrate. As the pore water resides at the grain contacts this leads to the hydrate exhibiting a cementing pore habit with the hydrate bearing sand exhibiting substantial cementation/cohesive strength (Waite et al. 2004). It is proposed that the role of hydrate in strength modification through cementation is analogous to that of water-ice in frozen soils. In the proximity of an abundant methane source, natural hydrate bearing sediments can exhibit cementing pore habit in sands (Booth et al. 1996).

As most hydrate-bearing sediments in nature are saturated with pore water and not methane gas, a number of researchers have used either the excess water method to form water-saturated hydrate bearing sands or utilized the excess gas method and subsequently replaced the methane gas with water after formation. In these instances, the hydrate exhibits a load-bearing habit where hydrate does not cement the grain contacts and interacts with the sediment by acting as a mineral grain (Waite et al. 2009). It is considered that saturating the sand with water after hydrate formation can cause partial dissociation/dissolution of hydrate (Hyodo et al. 2013a). It is often assumed that in nature most hydrates exhibit this behavior.

The geomechanical behavior of hydrate bearing sands depends on several test parameters, such as effective confining pressure, pore pressure, strain rate, temperature, drainage (Winters et al. 2004) as well as the resultant hydrate morphology after formation (Priest et al., 2009). Understanding the influence of each parameter and their relevance to conditions prevailing in natural hydrate deposits is indispensable to hydrate research. Strength of hydrate bearing sands increases with effective confining pressure (Miyazaki et al. 2010; Yoneda et al. 2015) with saturated hydrate bearing sands having a lower strength increase than those saturated by methane gas (Hyodo et al. 2013a; Miyazaki et al. 2011). Cementing hydrates lead to the development of a peak strength with significant post-peak strain-softening, which can be suppressed at higher confining pressures (Miyazaki et al. 2010). In contrast, saturated hydrate bearing sands do not exhibit any appreciable peak and present a strain-hardening behavior with increasing strain. Within a Mohr-Coulomb framework, it was suggested that hydrate within the pore space increased cohesion, c', of the sand but without altering the friction angle, ϕ' (Hyodo et al. 2013b), although Yoneda et al., (2016) presented results suggesting that hydrate also increased ϕ'.

This paper presents and compares the results of a comprehensive study into the mechanical behavior of different sands, namely gas and water-saturated hydrate-bearing sands as well as frozen sands. In the selection of the host sediment, due consideration was given to the moisture retention capacity of the host sediment to ensure that hydrate and ice were homogenously distributed through the sand. Small strain stiffness was measured throughout the hydrate formation, subsequent saturation, as well as hydrate dissociation using a resonant column. Drained triaxial shear tests were conducted on the various specimens to determine their deformation and strength characteristics and compare similarities or differences.

2. MATERIALS AND METHODS

2.1. Host sediment

To achieve a homogenous distribution of water for subsequent hydrate or ice formation the host sand must have the capacity to hold the free water at particle contacts and overcome the effects of gravity that can lead to segregation of the water. Two types of sands were evaluated; Ottawa sand 50/70 (OS) and Wisconsin sand 50/140 (WS), with each sand's grain size distribution and index properties presented in Figure 1. To evaluate the water retention capacity of each sand, different volumes of water were thoroughly mixed with the sand and tamped into a cylindrical mold (90mm dia. by 110mm in height). The sand specimens were sealed in plastic bags for ~3hrs before being cut into 5 equal layers down the height of the specimen and the water content of each layer subsequently determined. Figure 2 presents the maximum moisture content for each specimen that gave a reasonably homogenous distribution, highlighting the much higher average saturations for the WS compared to OS: Therefore, WS was used as the host sediment for all tests in this study.

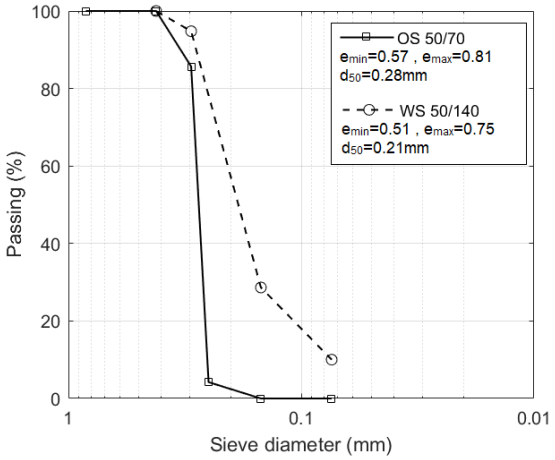

Figure 1. Grain-size distribution of host sand.

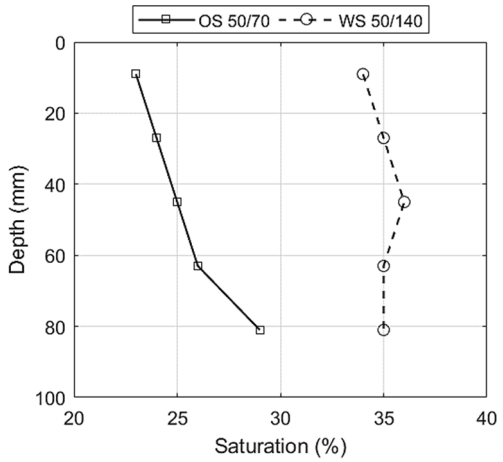

Figure 2. Moisture distribution characteristics for different sands.

2.2. Apparatus

The geomechanical behavior of the sand specimens was evaluated in the Environmental Triaxial Automated System (ETAS) manufactured by GDS Instruments. The ETAS is a load-frame based high-pressure triaxial system with temperature control. An external glycol cooling unit connected to a coiled tube that runs along the inner walls of the triaxial cell allows the cell temperature to be controlled between -30°C to +65°C.

The triaxial cell is equipped with a Hardin-type resonant column (RC) drive head that can be used to vibrate the specimen at its resonant frequency from which the small-strain shear modulus, G_{max}, of the specimen can be determined. The RC drive head is connected via a thin tubular aluminum column to the top pedestal that allows RC tests to be performed with up to 2kN of anisotropic axial load applied to the specimen. At axial stresses < 2kN the thin aluminum bar shortens, and the pedestal comes into contact with the RC drive head. This allows up to 50 kN of an axial load to be applied to the specimen during triaxial compression. The triaxial cell is designed for a maximum allowable confining pressure of 20MPa. Pneumatic gas pressure controllers and screw-driven pressure/volume controllers allow independent control of cell pressure and back pressure at the top and bottom of the specimen.

An additional cooling bath was used to control the temperature of water entering the specimen during the saturation phase for water-saturated hydrate bearing specimens to reduce potential dissociation of hydrate during this phase (after hydrate formation). A gas-water mixer tank was also used to saturate the pore water with methane before saturating the specimen.

2.3. Specimen preparation

Sand specimens were formed by mixing Wisconsin 50/140 sand with a predetermined volume of water corresponding to the target hydrate/ice saturation, before being compacted in 10 equal layers within a gas-impermeable butyl membrane held inside a split mold that was fixed around the (removable) bottom pedestal of the triaxial cell. About 100gm of sand of the moist sand was used to determine the initial moisture content of each specimen.

Once formed, the specimen was placed in the triaxial cell and subjected to an effective confining pressure (σ_3') of 200kPa. For frozen sands, the cell temperature was set to -9°C. Specimens were maintained at these conditions for 24hrs before testing. For hydrate bearing specimens, the cell gas pressure (nitrogen) and methane gas pore pressure were initially simultaneously raised to 2.7MPa and 2.5MPa, respectively, at a rate of 100kPa/min (Stage 1: Figure 3). At this point, the temperature of the system was set to a 2 °C (Stage 2: Figure 3). It took ~12hrs for the specimen to reach its target temperature. Then, the cell pressure and pore pressure were raised to 6.2MPa and 6MPa, respectively, which was well inside the PT conditions for hydrate stability (Stage 3: Figure 3). Specimens were held under these conditions for up to 26hrs to allow complete hydrate formation. The purpose of using two stages of pressurization during the hydrate formation process was to ensure uniform hydrate formation conditions ($+2 \pm 0.25$ °C), since raising pressure and lowering the temperature would lead to different formation conditions over an extended time period.

To saturate the hydrate bearing specimen (WHS1) with water, the cell pressure and the pore pressure were reduced to 3.85MPa and 3.35MPa after hydrate formation, respectively. Cooled methane-saturated water was passed through the specimen. In total, ~three volumes of the pore space over a period of 10hrs were passed through the specimen. After saturating the specimen, the cell pressure and back pressure were increased to 7MPa and 6MPa respectively. The specimen was maintained under these conditions for 1.5hr to allow any gas bubbles to dissolve or convert to hydrate.

For gas-saturated specimens, the hydrate saturation (S_h) was calculated from the initial water content (Ghiassian and Grozic 2013). For the water-saturated specimens, S_h was estimated from the volume of gas collected after dissociating the hydrate at the end of the test. A summary of the index properties and test parameters for all specimens tested is given in Table 1. Four different sands were tested, i.e., base sands, frozen sands (FS), hydrate sands (HS) and water-saturated hydrate bearing sands (WHS).

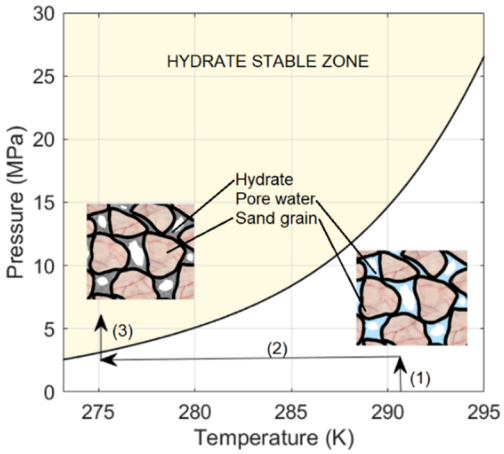

Figure 3. Pressure-temperature stability boundary for hydrate in pure water systems and formation history.

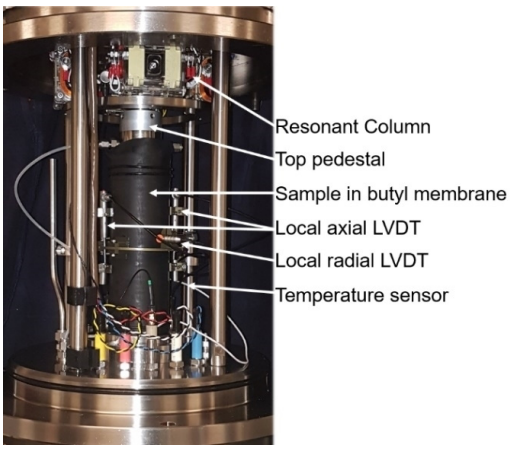

Figure 4. Specimen assembly in the triaxial cell.

		Specimen properties						Test parameters		MC strength parameters			
										Peak		Residual	
	S.N.	S (%)	S_h (%)	S_i (%)	e	γ_d (kN/m^3)	$\overline{S_h}$, $\overline{S_i}$ (%)	σ_3' (kN/m^3)	u (kN/m^3)	c' (MPa)	ϕ' (deg)	c' (MPa)	ϕ' (deg)
Base Sand	1	38.5	-	-	0.54	16.83		0.5	0	0	35.22	0	35.22
	2	38.6	-	-	0.54	16.91		1	0				
	3	38.2	-	-	0.54	16.85		2	0				
HS	1	17.4	20	-	0.54	16.87		0.5	6	1.38	32.47	0.37	34.12
	2	17.4	20	-	0.55	16.77	19.8	1	6				
	3	16.9	19.4	-	0.55	16.79		2	6				
	4	38	43.7	-	0.55	16.8		0.5	6	1.97	36.64	0.36	40.13
	5	38.6	44.4	-	0.55	16.8	44.2	1	6				
	6	38.8	44.5	-	0.54	16.92		2	6				
FS	1	16.8	-	18.3	0.55	16.77		0.5	0	0.34	39.01	0.074	39.15
	2	16.5	-	18	0.56	16.62	18.2	1	0				
	3	16.7	-	18.2	0.54	16.84		2	0				
	4	37.2	-	40.5	0.57	16.52		0.5	0	1.27	38.7	0.36	40.74
	5	37.5	-	40.8	0.57	16.59	40.7	1	0				
	6	37.4	-	40.7	0.56	16.67		2	0				
WHS	1	38.2	37.9		0.53	17.04		1	6	-	-	-	-

Table 1. Specimen index properties, test parameters, and strength parameters from Mohr-Coulomb failure theory. Notes: γ_d – Dry unit weight, e – Voids ratio, u – pore pressure, c' – Cohesion, ϕ' – Friction angle, $\overline{S_h}$ – Average hydrate saturation, $\overline{S_i}$ – Average ice saturation.

2.4. Testing procedures

Resonant column tests were conducted throughout the hydrate formation and subsequent saturation period for the HS and WHS specimens, to determine G_{max} of the specimens. The measured resonance frequency in conjunction with other system parameters was used to calculate G_{max} (ASTM D4015-17).

To obtain large-strain strength properties, specimens were sheared under consolidated drained conditions. For gas-saturated HS, the back pressure was maintained at 6MPa with the cell pressure adjusted to match the desired σ_3'. For FS, the back pressure was maintained at atmospheric pressure. Specimens were sheared at an axial strain rate of 0.1%/min. Two local axial and one radial linear variable displacement transducers (LVDT) were used to record the local deformations in the middle third of the specimen (See Figure 4 for specimen assembly). Specimens were sheared up to a total axial strain of 11%.

3. RESULTS AND DISCUSSION

3.1. Shear modulus, G_{max}

The small-strain shear modulus of the hydrate bearing specimen was evaluated using the resonant frequency obtained during resonant column tests. Figure 5 shows the evolution of shear modulus during the hydrate formation stage plotted for specimen HS4 (all hydrate specimens followed similar trends). G_{max} increases rapidly during the first 15hrs of formation. After about 24hrs, G_{max} appears to approach an asymptotic value. Even at the end of the formation period, G_{max} appears to be increasing, though at a very small rate. This could be related to incomplete hydrate formation, potential compaction of the specimen due to repeated RC tests resonance, or increasing hydrate crystal growth-size through Ostwald-ripening (Spangenberg et al. 2015). One test was conducted (S_h=44.5%) where hydrate formation was monitored over 36hrs (not reported herein). Compared to HS4 (which was incubated for 24hrs), the peak strength increased by less than 0.85%. Therefore, hydrate formation was limited to 24hrs time period.

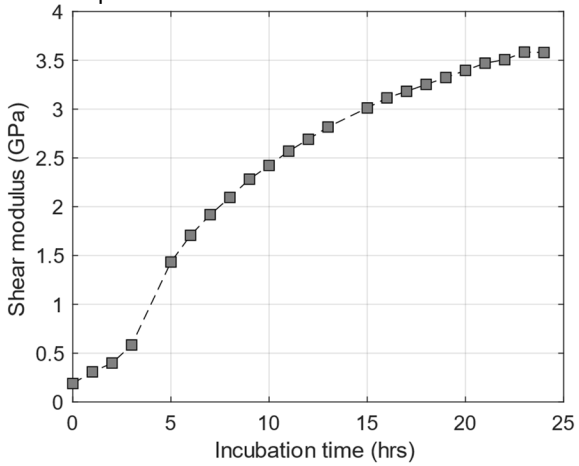

Figure 5. Evolution of shear modulus during hydrate formation.

The changes in G_{max} during hydrate formation and subsequent water saturation of the pore space for WHS1

is shown in Figure 6. It can be seen that during formation, the change in G_{max} initially follows a similar trend as that observed for HS4 (see Figure 5). Before saturating WHS1, the specimen's PT conditions were brought close to the hydrate stability boundary. A slight reduction in G_{max} was observed due to the pore-pressure drop. Hyodo et al. (2013) made similar observations and reported reduced stiffness and strength for HS at lower pore pressures. However, as the specimen was subsequently saturated with water, a significant loss in G_{max} can be observed. After flowing 350 ml of water (three volumes of the pore space) through the specimen, G_{max} had dropped by 56%. This loss of stiffness could be due to partial hydrate dissociation at the grain contacts (Figure 6-C), which would result in a major loss of structural (cementation) strength in the specimen.

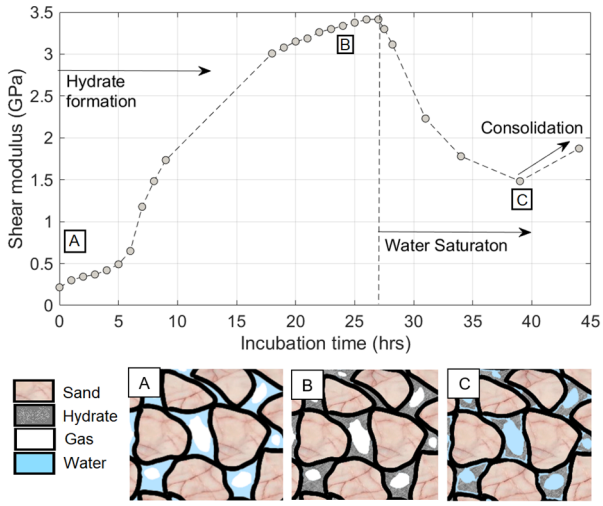

Figure 6. Variation in shear modulus during hydrate formation and subsequent saturation. (A) Partially saturated sand. (B) Gas-saturated hydrate bearing sand. (C) Water-saturated hydrate bearing sand with partial hydrate dissociation at the grain contacts

3.2. Strength

The results of triaxial shear tests for the different sands tested are presented in terms of stress-strain histories through Figure 7-10. Each stress-strain history consists of a plot of deviator stress and radial strain, ϵ_r (response variables) versus axial strain, ϵ_a (control variable). Axial strain values up to 3.5% were obtained from the local axial LVDT's, while above this value are obtained from the global LVDT. The Mohr-Coulomb failure theory was adopted to calculate the strength parameters, cohesion (c') and friction (ϕ'). The cohesion and friction were calculated for both peak strength and residual states (Table 1). Figure 7 shows the triaxial stress-strain response of the baseline sand specimens for comparison with the behavior of FS and HS specimens.

3.2.1. Influence of ice saturation

The stress-strain histories for the FS specimens are presented in Figure 8. It can be seen that all FS specimens

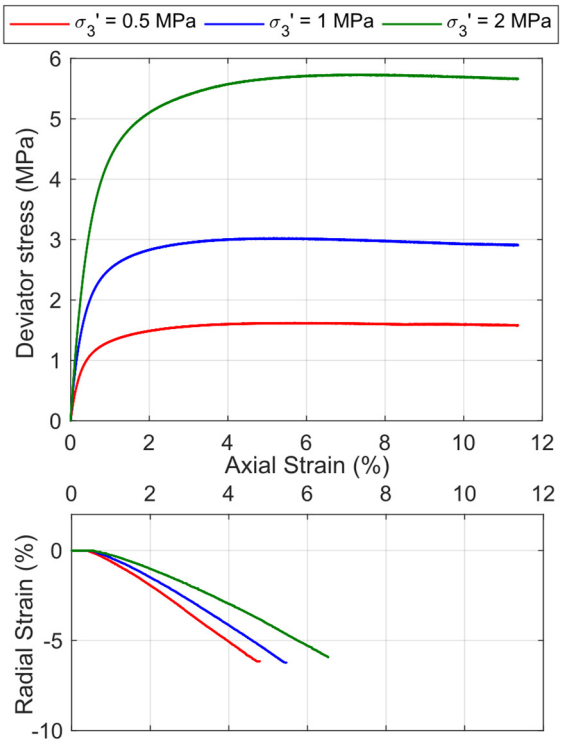

Figure 7. Stress-strain history during triaxial shear of base-sand specimens.

exhibit strain softening behavior after reaching a peak stress, with the magnitude of peak stress and subsequent strain softening increasing with higher average ice saturation ($\bar{S}_i$). In addition, peak strength occurs between 2.3% and 3.4% axial strain for specimens with ice saturation ($\bar{S}_i$) of 18.2% and between 3.1% and 3.4% for $\bar{S}_i$=40.7%. Moreover, the slope of the stress-strain curve (large-strain Young's modulus, E_T) is independent of σ_3' for $\bar{S}_i$=40.7% up to an axial strain of 0.075% and increases thereafter with increasing σ_3'. In contrast, E_T appears stress dependent from the beginning of the test for $\bar{S}_i$=18.2%. c' and ϕ' calculated for each average ice saturation are provided in Table 1. It can be seen that c' increased sharply with increasing ice saturation of the specimens, although only minor increases in ϕ' were observed both at the peak and residual states. In addition to potentially cementing the soil grains, ice can increase the strength (and cause minor changes in ϕ') by forming wedges between soil grains (increasing dilation) and influence the friction angle by acting as finer solid fraction after the formation of shear band. Some apparent residual cohesion was also observed at the residual state. At the residual state, the resistance should theoretically be only frictional, however, the formation of 3-dimensionally oriented shear bands can impart stability and appear as apparent cohesion according to classical Mohr-Coulomb failure theory (Wong 2001).

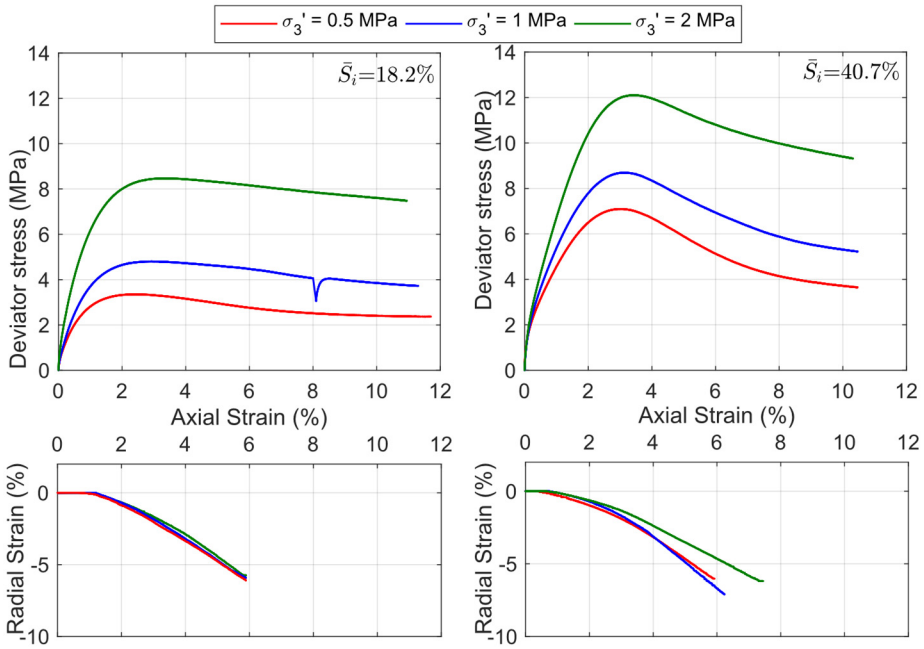

Figure 8. Stress-strain history during triaxial compression of frozen sand specimens.

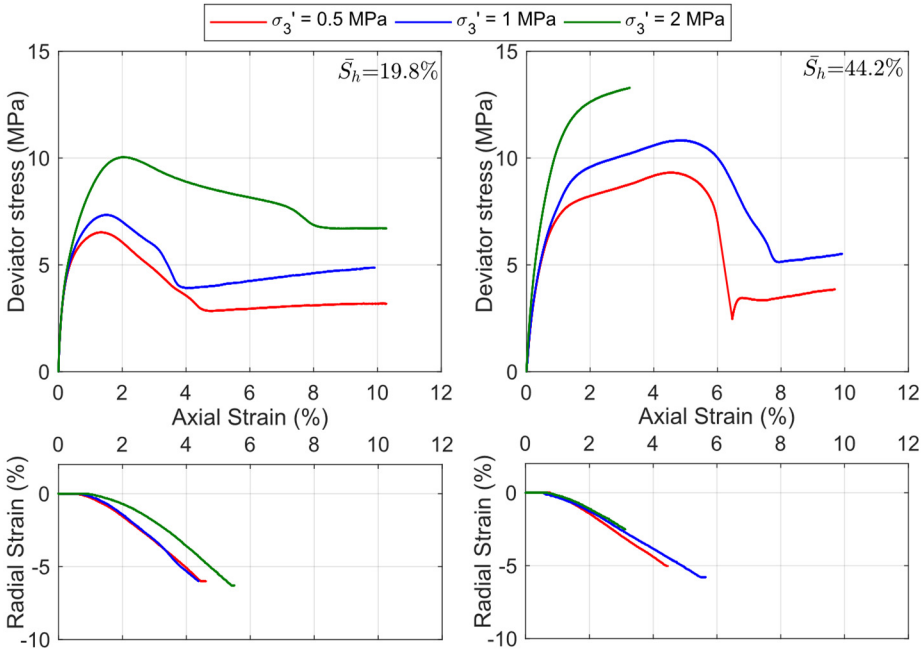

Figure 9. Stress-strain history during triaxial compression of hydrate bearing sand specimens.

3.2.2. Influence of hydrate saturation

The results of triaxial shear tests for gas-saturated HS specimens are presented in Figure 9. Except for HS6, E_T of all HS specimens was independent of σ_3' up to 0.2% axial strain. Full axial strain could not be achieved for HS6 because the load frame reached its maximum capacity. For all other specimens, peak strength was observed at axial strain between 1.4-2.0%. The average initial E_T for average hydrate saturation ($\bar{S}_h$) of 19.8% and 44.2% was 4.06GPa and 2.01GPa respectively. If the complete conversion of water into hydrate is assumed, the volume of hydrate is about 13% greater than the original volume of the pore water. Therefore, at higher $\bar{S}_h$, this expansion could reduce the intergranular stresses at the particle contacts and may result in a lower initial E_T.

All HS specimens exhibited severe strain softening behavior when compared to that for the FS specimens. Specimens with high hydrate saturations ($\bar{S}_h$=44.2%) reached an initial yield point at about 1.5% axial strain

where the rate of increase in strength reduced, although the overall magnitude of strength continued to increase up to a peak stress that occurred around ~5% axial strain followed by a structural collapse of the soil. We postulate that at the initial yield point, the strain was localized through potential de-bonding of hydrate from the grain surface without significant yielding of the hydrate crystals. At the collapse point, significant yielding of the hydrate may have occurred leading to the sharp reduction in deviator stress to a residual value. Comparing the post-peak response of HS3 with HS1 and HS5 with HS4, it appears that the occurrence of the residual state was delayed by increasing confining stress. This indicates that after the collapse, most of the cemented bonds were destroyed along the shear band and the behavior of the specimens was controlled by friction mobilized along the shear band. Specimen HS4 was extracted from the cell after shearing with some hydrate intact. The shear plane coincided with the top pedestal and minor compression at the top edge of the lower sheared block was observed. This could explain the slight increase in stress after the residual state for HS4 between axial strains of 7%-8%. Lower radial strains were observed at higher effective confining pressure for all specimens.

The values for c' and ϕ' at the peak and residual states are listed in Table 1. Both c' and ϕ' appear to contribute to the peak shear strength. At lower confining pressures, the peak strength was primarily related to c' (due to cementation of the soil grains at the contacts by the hydrate). Compared to the baseline sand specimen, ϕ' increased at higher hydrate saturation and was reduced at lower hydrate saturation. A small value of residual cohesion was also observed which can be attributed to the formation of 3D shear bands and platen effects.

3.2.3. Influence of water saturation on hydrate bearing sands

Specimen WHS1 was saturated with water after the formation of hydrate. Figure 10 shows the results of a triaxial shear test conducted after the saturation stage. The specimen exhibited a peak strength of 4.66MPa at an axial strain of 1.7% followed by progressive strain softening. The peak strength is only 43% of the peak strength recorded for gas-saturated HS5 (formed and tested under similar conditions and initial hydrate saturation). From the plot of volumetric strain vs. axial strain, a small initial compression of the specimen was observed up to 0.34% axial strain followed by dilation. Peak dilation rate ($\frac{\epsilon_v}{\epsilon_a}$) was achieved at ~2.6% axial strain. One of the pressure/volume controllers reached its maximum capacity and specimen shearing had to be momentarily stopped to refill the controller (as observed by the reduction in deviator stress at an axial strain of ~7%).

As only one WHS test was completed we could not determine c' and ϕ' directly. Therefore, assuming a peak ϕ' of 35° (since ϕ' is reasonably independent of hydrate saturation) then according to the Mohr-Coulomb theory, the peak c' = 0.27MPa. This equates to 13.2% of the peak c' observed for gas-saturated HS that were formed with similar initial water saturation.

Assuming that the initial pore water had completely converted to hydrate during formation, then the hydrate saturation should have been 43.9%. However, using the volume of methane gas collected after dissociation of the hydrate, the hydrate saturation of the specimen was found to be 37.9%. It is likely that some of the hydrate dissociated during the water saturation process. However, the peak strength and cohesion have been reduced substantially. The peak strength of gas-saturated HS2 with S_h=20% was 57% higher than water-saturated WHS1 with S_h=37.9%. This indicates that just as hydrate forms first at the contacts, hydrate dissociation appears to occur at the contacts as well. Thus, a minor loss of hydrate gives rise to a significant loss in strength of the hydrate bearing sand. This finding has serious implications to the behavior of hydrate-bearing sediment samples recovered from natural reservoirs, where the slightest disturbance during extraction and transportation could substantially influence the measured strength and stiffness characteristics.

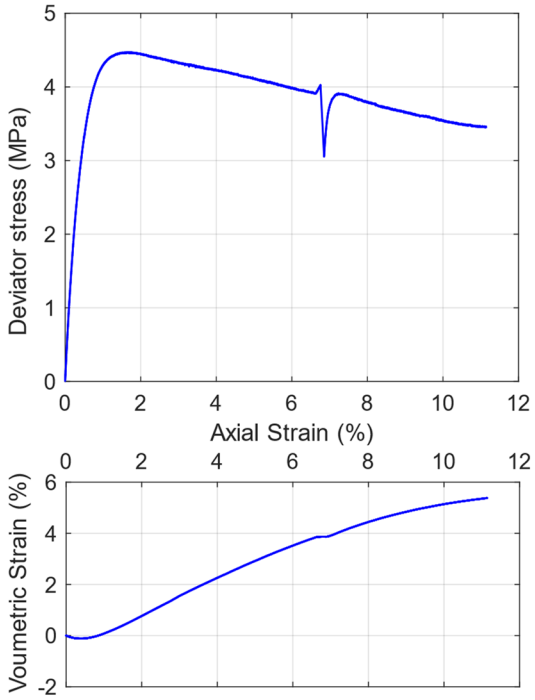

Figure 10. Stress-strain history during triaxial shear of water-saturated hydrate bearing specimen

3 CONCLUSIONS

The geomechanical properties of sand with different forms of cementation within the pore space, namely frozen sands, gas-saturated and water-saturated hydrate bearing sands, were studied and compared with the properties of the host sand. The findings of this study can be summarized as follows.

Comparing gas-saturated hydrate bearing sands and frozen sands, both hydrate and ice substantially increase the strength of sand and give rise to significant post-peak strain-softening behavior. The strength increase due to hydrate is always much greater than that for ice when compared for similar saturations of the pore space. The

principle source of peak strength is cementation (cohesion), however, both hydrate and ice also act as a solid fraction in the sediment structure and influence friction angle. Deformation characteristics of both frozen and hydrate bearing sands vary profoundly. At higher hydrate saturations, the hydrate undergoes substantial plastic deformation and delays the peak strength and subsequent collapse.

Comparing water-saturated and gas-saturated hydrate bearing sands, the minor loss of hydrate during saturation of the pore space, possibly through dissociation of hydrate at grain contacts, can cause major loss of strength and stiffness.

4 REFERENCES

Booth, J., Rowe, M., Fischer, K., 1996. Offshore Gas Hydrate Sample Database: With an Overview and Preliminary Analysis. Mar. Geol. 1, 1–31.

Collett, T.S., Johnson, A.H., Knapp, C.C., Boswell, R., 2009. Natural Gas Hydrates: A Review. Nat. gas hydrates—Energy Resour. potential Assoc. Geol. hazards AAPG Mem. 89, 146–219.

Ghiassian, H., Grozic, J.L.H., 2013. Strength behavior of methane hydrate bearing sand in undrained triaxial testing. Mar. Pet. Geol. 43, 310–319.

Handa, Y.P., Stupin, D.Y., 1992. Thermodynamic properties and dissociation characteristics of methane and propane hydrates in 70-.ANG.-radius silica gel pores. J. Phys. Chem. 96, 8599–8603.

Hyodo, M., Kajiyama, S., Kato, A., Nishimura, A., Nakata, Y., Yoshimoto, N., 2015. Effect of fines on mechanical properties of methane hydrate bearing sands. Isfog 2015 969–974.

Hyodo, M., Yoneda, J., Li, Y., Nakata, Y., Yoshimoto, N., Nishimura, A., Song, Y., 2013a. Mechanical behavior of gas-saturated methane hydrate bearing sediments. J. Geophys. Res. Solid Earth 118, 5185–5194.

Hyodo, M., Yoneda, J., Yoshimoto, N., Nakata, Y., 2013b. Mechanical and dissociation properties of methane hydrate bearing sand in deep seabed. Soils Found. 53, 299–314.

Hyodo, M. and Yoshimoto, N., 2013. Shear strength and deformation of methane hydrate bearing sand with fines, in: Proceedings of the 18th ICSMGE. pp. 1011–1014.

Kvenvolden, K.A., 1993. Gas hydrates—geological perspective and global change. Rev. Geophys. 31, 173–187.

Miyazaki, K., Masui, A., Sakamoto, Y., Aoki, K., Tenma, N., 2011. Triaxial compressive properties of artificial methane - hydrate - bearing sediment 116, 1–11.

Miyazaki, K., Masui, A., Sakamoto, Y., Tenma, N., Yamaguchi, T., 2010. Effect of confining pressure on triaxial compressive properties of artificial methane hydrate bearing sediments. Offshore Technol. Conf. 1823–1831.

Miyazaki, K., Yoshihiro, E., Tenma, N., Yamaguchi, T., 2015. Effects of Particle-Size Distribution on the Viscoelasticity of Artificial Methane-Hydrate bearing Sand 25, 112–119.

Moridis, G.J., Collett, T.S., Dallimore, S.R., Satoh, T., Hancock, S., Weatherill, B., 2004. Numerical studies of gas production from several CH4 hydrate zones at the Mallik site, Mackenzie Delta, Canada. J. Pet. Sci. Eng. 43, 219–238.

Priest, J.A., Rees, E.V.L., Clayton, C.R.I., 2009. Influence of gas hydrate morphology on the seismic velocities of sands. J. Geophys. Res. Solid Earth 114, 1–13.

Santamarina, C.J., Dai, S., Jang, J., Terzariol, M., 2012. Pressure core characterization tools for hydrate bearing sediments. Sci. Drill. 44–48.

Spangenberg, E., Kulenkampff, J., Naumann, R., Erzinger, J., 2005. Pore space hydrate formation in a glass bead sample from methane dissolved in water. Geophys. Res. Lett. 32, 1–4.

Spangenberg, E., Priegnitz, M., Heeschen, K., Schicks, J.M., 2015. Are laboratory-formed hydrate bearing systems analogous to those in nature? J. Chem. Eng. Data 60, 258–268.

Stern, L.A., Kirby, S.H., Durham, W.B., 1996. Peculiarities of Methane Clathrate Hydrate Formation and Solid-State Deformation, Including Possible Superheating of Water Ice 273, 1843–1848.

Waite, W.F., Santamarina, J.C., Cortes, D.D., Dugan, B., Espinoza, D.N., Germaine, J., Jang, J., Jung, J.W., Kneafsey, T.J., Shin, H., Soga, K., Winters, W.J., Yun, T.S., 2009. Physical properties of hydrate bearing sediments. Rev. Geophys. 47, 1–38.

Waite, W.F., Spangenberg, E., 2013. Gas hydrate formation rates from dissolved-phase methane in porous laboratory specimens 40, 4310–4315.

Waite, W.F., Winters, W.J., Mason, D.H., 2004. Methane hydrate formation in partially water-saturated Ottawa sand. Am. Mineral. 89, 1202–1207.

Winters, W.J., Waite, W.F., Dugan, B., Mason, D.H., Coastal, I.A.P., Program, M.G., 2004. Strength and Physical Properties of Sediment Containing Laboratory-Formed and Natural Gas Hydrate 89, 2543.

Wong, R.C.K., 2001. Strength of two structured soils in triaxial compression. Int. J. Numer. Anal. Methods Geomech. 25, 131–153.

Yoneda, J., Jin, Y., Katagiri, J., Tenma, N., 2016. Strengthening mechanism of cemented hydrate bearing sand at microscales 1–9.

Yoneda, J., Masui, A., Konno, Y., Jin, Y., Egawa, K., Kida, M., Ito, T., Nagao, J., Tenma, N., 2015. Mechanical properties of hydrate bearing turbidite reservoir in the first gas production test site of the Eastern Nankai Trough. Mar. Pet. Geol. 66, 471–486.